



**HAL**  
open science

# Reduced order modeling for the prediction of combustion instabilities in liquid rocket engines: coaxial injection response and acoustic damping modeling

Alexandre Fougne, Schmitt Thomas, Sebastien Ducruix

## ► To cite this version:

Alexandre Fougne, Schmitt Thomas, Sebastien Ducruix. Reduced order modeling for the prediction of combustion instabilities in liquid rocket engines: coaxial injection response and acoustic damping modeling. EUCASS-CEAS 2023 10th European Conference for Aerospace Sciences (EUCASS)- 9th CEAS Conference, EUCASS - CEAS, Jul 2023, Lausanne, Switzerland. hal-04184450

**HAL Id: hal-04184450**

**<https://hal.science/hal-04184450>**

Submitted on 21 Aug 2023

**HAL** is a multi-disciplinary open access archive for the deposit and dissemination of scientific research documents, whether they are published or not. The documents may come from teaching and research institutions in France or abroad, or from public or private research centers.

L'archive ouverte pluridisciplinaire **HAL**, est destinée au dépôt et à la diffusion de documents scientifiques de niveau recherche, publiés ou non, émanant des établissements d'enseignement et de recherche français ou étrangers, des laboratoires publics ou privés.

DOI: ADD DOINUMBER HERE

# Reduced order modeling for the prediction of combustion instabilities in liquid rocket engines: coaxial injection response and acoustic damping modeling

FOUGNIE Alexandre<sup>\*,\*\*</sup>, SCHMITT Thomas<sup>\*†</sup> and DUCRUIX Sébastien<sup>\*</sup>

<sup>\*</sup>Laboratoire EM2C, CNRS, CentraleSupélec, Université Paris-Saclay, Gif-sur-Yvette, France

<sup>\*\*</sup>CNES, Direction Technique et Numérique, Paris, France

thomas.schmitt@centralesupelec.fr

<sup>†</sup>Corresponding author

## Abstract

A reduced-order code based on a Galerkin modal expansion of the pressure oscillations is presented to predict high frequency combustion instabilities in liquid rocket engines. Models to account for acoustic damping are proposed, such as nozzle, thermal or viscous losses. A combustion source term modeling the fuel inflow modulation of a coaxial injection unit through a flame transfer function is derived. A first application is made on the NPCC test bench, retrieving LES data with a nonlinear representation of the damping. Then the BKD combustor of DLR is simulated, and first comparisons with LES results are proposed.

## 1. Introduction

High-frequency combustion instabilities, also called thermoacoustic instabilities, have been a recurring challenge in the design of liquid rocket engines (LRE) since the beginning of the space era.<sup>1,2</sup> These instabilities arise from a coupling between the combustion chamber acoustics, the injection dynamics and the flames unsteady heat release. This coupling results in pressure oscillations and modifications of the thermal loading that reduce the engine's propulsive performances and may lead to its destruction.<sup>3</sup> Due to the large number of phenomena potentially involved, combustion instabilities are still not fully understood and fairly difficult to predict. Consequently, many studies on flame and injection behaviors are carried out either on laboratory test benches<sup>4</sup> or representative rocket engines<sup>5</sup> using experiments and high-fidelity simulations.<sup>6,7</sup> However, these simulation tools are ill-suited for predesign stages, requiring too much time and resources. Reduced-order approaches<sup>8</sup> are thus gaining an increasing interest, enabling to rapidly test multiple configurations and loading points. Still, these methods require more modeling efforts than large eddy simulations (LES).

Therefore, in collaboration with CNES and ArianeGroup, the EM2C laboratory is developing the StaHF<sup>9</sup> (Stability High Frequency) code, based on a Galerkin modal expansion of the pressure oscillations on the acoustic eigenmodes<sup>10</sup> of the system, reviewed in Sec. 1. Models converting the flame responses into pressure fluctuations have been derived along with excitation terms.<sup>9,11</sup> To extend the StaHF capacities and perform simulations with fewer adjustment parameters, the modeling of the leading acoustic damping phenomena are proposed in Sec. 2, as viscous, thermal, nozzle and injection plate losses or nonlinear energy transfer between modes. Also, the previous flame response models are completed with a model for of the annular fuel modulation in Sec. 3. Applications are made on a cold flow test bench, the NPCC,<sup>11</sup> in Sec. 4 and on the BKD<sup>5</sup> combustor from DLR in Sec. 5.

## 2. Reduced-Order Modeling

Reduced-order modeling (ROM) aims at describing the main couplings involved in thermoacoustic instabilities with a simplified set of physical relations, decreasing the numerical resources required.<sup>8</sup> Several approaches have been applied to thermoacoustic instabilities, as the use of Green's functions,<sup>12</sup> the decomposition in an acoustic network with Riemann invariant,<sup>13</sup> or linearized solvers, as Helmholtz or LEE solvers.<sup>14</sup> The method chosen for StaHF is a Galerkin expansion,<sup>9,10</sup> that permits to handle the complexity of the engine geometry and to separate the temporal aspect from the spatial modal structure while working in temporal space.

## 2.1 Modal expansion of pressure oscillations

StaHF relies on a modal expansion<sup>10</sup> of the pressure oscillations  $p'(\mathbf{x}, t)$ , also called Galerkin approach. The oscillations are projected onto the acoustic eigenmodes  $\Psi_n(\mathbf{x})$  of the engine so that

$$p'(\mathbf{x}, t) = \sum_{n=1}^{\infty} \eta_n(t) \Psi_n(\mathbf{x}), \quad (1)$$

with  $\eta_n$  the temporal evolution of the  $n^{\text{th}}$  mode and  $\Psi_n$  its spatial structure. It is supposed that the modes  $(\Psi_n)_{n \geq 0}$  form an orthogonal base, verifying

$$\int_V \Psi_n \Psi_m dV = \Lambda_n \delta_{nm} \text{ with } \Lambda_n = \int_V \Psi_n^2 dV, \quad (2)$$

with  $\Lambda_n$  the norm of the  $n^{\text{th}}$  mode. This approach enables to isolate the temporal component of the oscillations from the spatial one

$$\gamma \bar{p} \nabla \cdot \left( \frac{1}{\bar{\rho}} \nabla \Psi_m \right) + \omega_m^2 \Psi_m = 0 \quad (3a)$$

$$\nabla \Psi_m \cdot \mathbf{n} = 0 \quad \text{or} \quad \Psi_m = 0 \quad \text{on the boundaries} \quad (3b)$$

where  $\gamma$  is the specific heat ratio,  $\bar{\rho}$  the mean density,  $\bar{p}$  the mean pressure and  $\omega_m = 2\pi f_m$  the mode's frequency. Eq. 3 is solved here using the Helmholtz solver AVSP<sup>14</sup> from Cerfacs, but it can be also solved analytically for simple geometries or using another acoustic tool. Eq. 3b is the boundary condition, where homogeneous Neumann or Dirichlet conditions can be applied. The formulation of Eq. 3 ensures the modes' orthogonality.

## 2.2 Modal amplitude differential equation

We start the development with from the conservation equations and the perfect gas equation of state that write

$$\frac{\partial \rho}{\partial t} + \nabla \cdot \rho \mathbf{u} = 0, \quad (4)$$

$$\rho \left( \frac{\partial \mathbf{u}}{\partial t} + \mathbf{u} \cdot \nabla \mathbf{u} \right) = -\nabla p, \quad (5)$$

$$\rho T \left( \frac{\partial s}{\partial t} + \mathbf{u} \cdot \nabla s \right) = \dot{q}, \quad (6)$$

$$p = \rho^\gamma e^{s/c_v}, \quad (7)$$

where  $T$  is the temperature,  $\mathbf{u} = (u_x, u_y, u_z)$  the velocity,  $s$  the entropy,  $\dot{q}$  the heat release rate and  $c_v$  the specific heat of the mixture at constant volume. A linear decomposition of the magnitudes is performed, so that for instance  $p$  is decomposed as  $p(\mathbf{x}, t) = \bar{p}(\mathbf{x}, t) + p'(\mathbf{x}, t)$ , with  $\bar{p}$  the temporal average and  $p'$  the fluctuations. Combining the four equations,<sup>10</sup> it comes the reactive acoustic equation:

$$\frac{\partial^2 p'(\mathbf{x}, t)}{\partial t^2} - \gamma \bar{p} \nabla \cdot \left( \frac{1}{\bar{\rho}} \nabla p'(\mathbf{x}, t) \right) = (\gamma - 1) \frac{\partial \dot{q}'}{\partial t} \quad (8)$$

that can be projected onto the modal base to obtain a differential equation verified by each mode<sup>15,16</sup>

$$\ddot{\eta}_m(t) + \omega_m^2 \eta_m(t) + \frac{1}{\Lambda_m} \int_S \bar{c}^2 p' \nabla \Psi_m \cdot \mathbf{n} - \bar{c}^2 \Psi_m \nabla p' \cdot \mathbf{n} dS = \frac{\gamma - 1}{\Lambda_m} \int_V \frac{\partial \dot{q}'}{\partial t} \Psi_m dV + S. \quad (9)$$

The third term of the LHS is a boundary term, noted hereafter  $S_Z^m$ , that can be rearranged to account for an impedance boundary condition. The first term of the RHS is the combustion source term, noted  $S_{comb}^m$ , representing the coupling between the unsteady heat release and the pressure fluctuations. The last term  $S$  represents complementary source terms that will be added when modeling other mechanisms. Further models are proposed below, by modeling the heat release  $\dot{q}'$  using acoustic quantities, by using the boundary term or by adding contributions into the conservation equation.<sup>16</sup>

### 3. Modeling of the damping phenomena

The source terms developed to account for acoustic losses are briefly reviewed in this section.

#### 3.1 Viscous and thermal losses

The viscous and thermal acoustic losses are often considered as negligible for liquid rocket engine applications, but often discussed for other applications like solid rocket boosters.<sup>17</sup> This is why a specific model is needed for StaHF to evaluate these losses for particular test benches, to confirm whether these losses can be neglected or not. Therefore, we seek to provide StaHF with models that allow the evaluation of viscous and thermal acoustic losses for all the acoustic modes used in the projection set.

##### Viscous losses

The viscous losses arise from a no-slip condition at the wall interface. To satisfy the  $u' \cdot n$  condition, the acoustic velocity takes a certain profile in the acoustic viscous boundary layer thickness  $\delta_{nu}^m$ , expressed as<sup>18</sup>

$$\delta_{nu}^m = \left( \frac{2\nu}{\omega_m} \right)^{1/2}, \quad (10)$$

with  $\nu$  being the kinematic viscosity. The velocity writes<sup>19</sup>

$$u'(x, y, t) = u_x(x) \left[ \exp\left( -\frac{y}{(1+j)\delta_{nu}^m} \right) \cos\left( \omega_m t - \frac{y}{\delta_{nu}^m} \right) - \cos(\omega_m t) \right], \quad (11)$$

with  $y$  the normal coordinate at the wall,  $u_x$  the transverse velocity at the plane, and  $u'$  the acoustic velocity along the  $x$  axis of a  $m^{\text{th}}$  harmonic motion. The velocity gradient between the bulk region and the wall leads to a shear stress, and consequently dissipation by friction.

The viscous stress tensor  $\underline{\tau}$  is kept in the derivation of the acoustic equation, and the modes are obtained with a zero velocity boundary condition. The modal differential Eq. 9 becomes, dropping the combustion source term and keeping the boundary term integral<sup>10</sup>

$$\ddot{\eta}_m(t) + \omega_m^2 \eta_m(t) - \frac{1}{\Lambda_m} \int_S \bar{c}^2 \Psi_m(\mathbf{x}_s) \nabla p' \cdot \mathbf{n}(\mathbf{x}_s, t) dS = -\frac{1}{\Lambda_m} \int_V \gamma \bar{p} \nabla \cdot \left( \frac{1}{\bar{\rho}} \nabla \cdot \underline{\tau}'(\mathbf{x}) \right) \Psi_m(\mathbf{x}) dV. \quad (12)$$

A boundary condition is applied on the gradient of the acoustic pressure field to convert the no-slip condition into a shear stress at walls:<sup>10</sup>

$$\nabla p' \cdot \mathbf{n}(\mathbf{x}_s, t) = \left( \nabla \cdot \underline{\tau}' \cdot \mathbf{n}(\mathbf{x}_s, t) \right). \quad (13)$$

After some manipulations,<sup>10,16</sup> it comes that the source term associated with the viscous losses at the walls is

$$S_v^m = -\frac{1}{\Lambda_m} \int_S \bar{c}^2 \left( \frac{\omega_m \nu}{2} \right)^{1/2} \frac{1}{\omega_m^2} (\nabla^t \Psi_m)^2 dS \dot{\eta}_m, \quad (14)$$

##### Thermal losses

Thermal losses are due to the isothermal wall condition, with acoustic oscillations considered as adiabatic. This adiabatic condition for acoustics is verified when  $\lambda_a$ , the acoustic wavelength, satisfies<sup>19</sup>  $\lambda_a > 2\pi D_{th}/c$ , where  $D_{th}$  is the thermal diffusivity. As for the acoustic velocity, there is a temperature gradient between the wall surface and the acoustic temperature oscillations outside the boundary layer. Thus an oscillating heat flux appears, leading to thermal losses linked with the acoustic thermal boundary layer thickness defined as

$$\delta_{th}^m = \left( \frac{2D_{th}}{\omega_m} \right)^{1/2}. \quad (15)$$

A similar approach to the one developed for viscous losses is proposed to account for thermal losses. Thermal effects are modeled keeping the dissipation term  $\nabla \cdot \mathbf{q}_f = -\nabla \cdot (\lambda_{th} \nabla T')$  in the derivation of Eq. 9, with  $\lambda_{th} = D_{th} \bar{\rho} c_p$  the thermal conductivity so that

$$\ddot{\eta}_m(t) + \omega_m^2 \eta_m(t) = \frac{1}{\Lambda_m} \int_V (\gamma(\mathbf{x}) - 1) \frac{\partial \nabla \cdot \mathbf{q}_f}{\partial t}(\mathbf{x}, t) \Psi_m(\mathbf{x}) dV. \quad (16)$$

Then the temperature Laplacian is linked to the pressure variations,<sup>19,20</sup> to transform the oscillating temperature component into a pressure oscillation leading to<sup>10,16</sup>

$$S_{th}^m = -\frac{1}{\Lambda_m} \int_S (\gamma - 1) \left( \frac{D_{th}\omega_m}{2} \right)^{1/2} \Psi_m^2 dS \dot{\eta}_m. \quad (17)$$

The viscous and thermal losses are implemented in StaHF and validations on pipes and boxes (not shown here) show good agreement with theoretical formulations.<sup>18</sup>

### 3.2 Nozzles losses

The nozzle losses are accounted for using an impedance boundary condition applied at the nozzle throat. The impedance is supposed to be a complex number and depend of the frequency, allowing to model non-compact nozzles. Therefore,  $Z = \mathcal{R} + j\mathcal{X}$  with  $\mathcal{R}$  the resistance and  $\mathcal{X}$  the reactance. The boundary source term of Eq. 9 can be rearranged using the boundary relation in the frequency domain

$$\hat{Z}(\mathbf{x}_s, \omega) = \frac{\hat{p}(\mathbf{x}_s)}{\bar{\rho} \bar{c} \hat{\mathbf{u}}(\mathbf{x}_s) \cdot \mathbf{n}}, \quad (18)$$

with  $\mathbf{x}_s$  located on the boundary, and the relation between the pressure and the velocity

$$\nabla p' \cdot \mathbf{n} = -j\omega \bar{\rho} \mathbf{u}' \cdot \mathbf{n}, \quad (19)$$

leading to the source term<sup>16</sup>

$$S_Z^m = -\frac{\mathcal{R}(\omega_m)}{\Lambda_m |Z(\omega_m)|^2} \int_{S_o} \bar{c}(\mathbf{x}_s) \Psi_m^2(\mathbf{x}_s) dS \dot{\eta}_m(t) + \frac{\mathcal{X}(\omega_m) \omega_m}{\Lambda_m |Z(\omega_m)|^2} \int_{S_o} \bar{c}(\mathbf{x}_s) \Psi_m^2(\mathbf{x}_s) dS \eta_m(t). \quad (20)$$

This relation is valid for  $|\mathcal{R}| > 1$ , but a similar source term can be obtained for  $|\mathcal{R}| < 1$ .<sup>16</sup> Validation steps are made on 2D geometries showing good agreement with analytic and numerical solutions (not shown here). However, for an impedance close to 1, the model does not correctly reproduce the asymptotic behavior. Nevertheless, the model gives an approximation of the nozzle losses for a reduced computational times, and is adapted to the Galerkin approach where modes must remain orthogonal. Another more complex method has been proposed by Laurent,<sup>8</sup> using a dual base approach.

### 3.3 Turbulence acoustic interaction

The turbulence acoustic interaction is characterized by at least two main phenomena. An acoustic wave impinging a turbulent zone, as a turbulent jet, or propagating through a turbulent medium undergoes energy losses due to the absorption of acoustic energy by the turbulence, and also a scattering effect. The scattering effect redirects part of the incident acoustic perturbation towards other frequencies and directions of propagation.<sup>21-23</sup> The acoustic energy is not actually lost because the energy remains acoustic, but the initial wave is weakened. The other phenomenon is absorption by turbulence. Passing through the turbulent medium, the acoustic wave stretches the vortices, that tend to bounce back to their initial state dissipating the energy.<sup>23-26</sup> The acoustic energy is lost through the deformation of the vortices, and converted into turbulent kinetic energy. Noir<sup>23</sup> and Howe<sup>26</sup> also mentioned that only eddies smaller than the acoustic wavelength contribute to the energy absorption, which is relevant to the combustion instability framework. The acoustic wavelength is of the size of the combustor and the eddies are much smaller, of the order of the injection unit radius and smaller. In this configuration, the acoustic frequency is large compared to the characteristic frequency of the turbulence, so that between two acoustic fluctuations, the vortices have the time to dissipate the energy gained during their deformation by the acoustic wave.

#### Term responsible for the absorption

The formulation of the term in the energy balance responsible for the turbulence acoustic interaction can be found using a triple decomposition<sup>27</sup> of the velocity as done by Reynolds,<sup>25</sup> where  $\mathbf{u} = \bar{\mathbf{u}} + \mathbf{u}' + \tilde{\mathbf{u}}$ ,  $\bar{\mathbf{u}}$  being the mean component,  $\mathbf{u}'$  the turbulent divergence-free velocity and  $\tilde{\mathbf{u}}$  the acoustic irrotational component. Using temporal averaging and phase averaging on the conservation equations, energy balances on  $\overline{\mathbf{u}' \cdot \mathbf{u}'}$  and  $\overline{\tilde{\mathbf{u}} \cdot \tilde{\mathbf{u}}}$  can be derived. The term  $\Pi$ ,

$$\Pi = \overline{\langle u'_i u'_j \rangle \frac{\partial \tilde{u}_i}{\partial x_j}}, \quad (21)$$

is common in both acoustic and turbulent velocity balance equations, associated with an exchange of energy between the turbulence and the acoustics.  $\langle \cdot \rangle$  is the phase averaging process. The term  $\Pi$  is identified as responsible for the absorption of acoustic waves by vortices. The damping coefficient can then be written as

$$\sigma_{turb} = -\frac{1}{2E_a} \bar{\rho} \int_V \overline{\langle u'_i u'_j \rangle \frac{\partial \tilde{u}_i}{\partial x_j}} dV. \quad (22)$$

### Extension of the Crow model for non-frozen turbulence

The model of Crow<sup>24</sup> is chosen for the reduced-order application, since it covers low and high frequency ranges and supposes a non-frozen turbulence.<sup>16</sup> The model is written to account for a particular acoustic velocity  $\tilde{\mathbf{u}}_m(x, t)$  where the modal expansion can be performed. It comes that

$$\Pi = \frac{12\pi}{5} \frac{\overline{u'^2(x)}}{\bar{c}^2(x)} \frac{f_i(x)}{1+f_i(x)} f_m |\tilde{\mathbf{u}}_m(x)|^2, \quad (23)$$

with  $f_m$  the acoustic frequency and  $f_i = \epsilon/(\overline{u'^2} \omega_m)$  a reduced frequency,  $\epsilon$  being the turbulence dissipation rate. Using the acoustic velocity as

$$|\tilde{\mathbf{u}}_m| = \frac{1}{\rho} \frac{1}{\omega_m^2} |\dot{\eta}_m| |\nabla \Psi_m|, \quad (24)$$

and the acoustic energy

$$E_a = 2 \int_V \frac{1}{2} \bar{\rho} |\tilde{\mathbf{u}}_m|^2 dV, \quad (25)$$

so that the damping rate is

$$\sigma_{turb} = \frac{12\pi}{10} \frac{\int_V \frac{\overline{u'^2(x)}}{\bar{c}^2(x)} \frac{f_i}{1+f_i} \frac{f_m}{\bar{\rho}^2} |\nabla \Psi_m|^2 dV}{\int_V \frac{1}{\bar{\rho}} |\nabla \Psi_m|^2 dV}. \quad (26)$$

This formulation enables to account for the mode structure. However, it demands an estimation of the velocities RMS and of the dissipation rate that are obtained using preliminary numerical computations.

### 3.4 Perforated plate losses

Perforated plates are widely used in industrial combustors and aeronautical combustion chambers to damp acoustic oscillations.<sup>28,29</sup> The hypothesis made in this work is that the injection plate acts as a perforated plate when it comes to acoustic damping. The plate schematized in Fig. 1 is considered. Holes are of diameter  $2a$ , uniformly spaced from a distance of  $d$ ,  $h$  is the thickness of the plate and the length of the back cavity is  $L$ . A bias flow  $u_0$  goes through the plate, which is the bulk flow in the longitudinal direction. The flow through an orifice creates a jet and the acoustic wave destabilizes the jet shear layer creating periodically vortices. This vorticity production absorbs some of the acoustic energy, weakening the acoustic wave.<sup>30-32</sup> For a detailed overview of the subject, please refer to Scarpato's articles.<sup>31,32</sup>

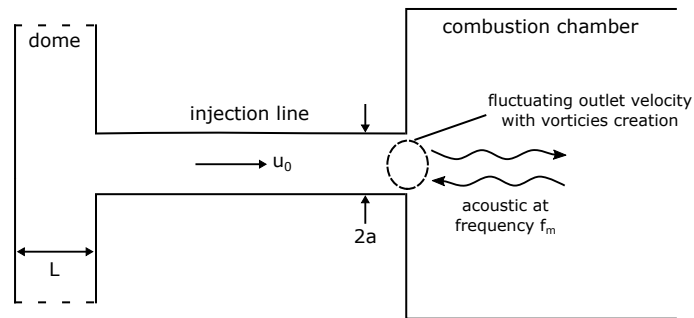


Figure 1: Representation of an injection line in the injection plate, with incoming acoustic waves.

The Rayleigh conductivity<sup>30</sup> of the plate that links the fluctuating pressure  $\tilde{p}_2 - \tilde{p}_1$  difference applied to the plate to the volume flow rate  $\tilde{q}$  through the injection unit is, considering the plate thickness<sup>33</sup>

$$K_R = \frac{j\omega_m \tilde{\rho} \tilde{q}}{\tilde{p}_2 - \tilde{p}_1} = 2a \left( \frac{1}{\gamma - j\delta} + \frac{2h}{\pi a} \right)^{-1}, \quad (27)$$

with  $\gamma - j\delta$  that is found using the relation

$$\gamma - j\delta = 1 + \frac{\frac{\pi}{2} I_1(S_t) e^{-S_t} - jK_1(S_t) \sinh(S_t)}{S_t \left[ \frac{\pi}{2} I_1(S_t) e^{-S_t} + jK_1(S_t) \cosh(S_t) \right]} \quad (28)$$

where  $I_1$  is the modified Bessel function of first kind and  $K_1$  is the modified Bessel function of second kind. It depends on the Strouhal number  $S_t = \omega_m a / u_0$ . The plate is characterized by a porosity  $\sigma = \pi a^2 / d^2$ . The Helmholtz number characterizing the back cavity influence is  $H_e = \omega_m L / \bar{c}$ , and the Mach number is  $M = u_0 / c$ . The impedance of the plate representing the conversion of the acoustics in vortices is

$$Z = j \left( \frac{\pi}{2} S_t \frac{M}{\sigma} \frac{1}{\gamma' - i\delta'} - \frac{1}{\tan(H_e)} \right). \quad (29)$$

To use this impedance into the reduced order formalism, we propose to use the boundary source term in Eq. 20, leading to

$$S_{plate}^m = - \frac{\mathcal{R}e(Z)}{\Lambda_m |Z|^2} \bar{c} \dot{\eta}_m(t) \sum_{n=1}^{N_{mf}} \Psi_m^2(\mathbf{x}_n) d^2. \quad (30)$$

## 4. Flame response models

Several combustion terms are developed to account for the different loading applied to the flames. The Spray Dynamic Modeling<sup>9</sup> allows to model the heat release due to the oscillating motion of the flames that follow the velocity acoustic field. Then, the pressure response model<sup>11</sup> accounts for the effect of the oscillating pressure on the flame.

### 4.1 Response of a coaxial injection unit

For an application to liquid rocket engines with coaxial injections, a model specific to the response of a coaxial injection unit to pressure oscillations is needed. Near velocity nodes, the flames are experiencing important pressure fluctuations at the outlet of the injection units leading to acoustic velocity fluctuations within the injectors, modulating the inflow velocity. This modulation produces perturbations for both the oxygen inner jet and fuel outer ring, increasing the turbulent mixing through vortices creation that are convected along the flame. Numerical simulations of such configurations has been performed<sup>34,35</sup> and led to the determination of Flame Transfer Functions (FTF) and saturation levels that could be used to obtain a Flame Describing Function. A model describing the physical phenomena has been of flame perturbation and stretching due to the vortex convection along the flame has been proposed by Nez.<sup>34</sup> Figure 2 represents a coaxial injection units with section changes in the injection line as in the BKD combustor.<sup>5</sup> Two response models are needed, one for the inner jet and one for the outer ring. Because waves going through the injector to the fuel dome are not reflected by the section change within the outer ring, the perturbation within the dome at the inlet and in the combustion chamber at the outlet can be supposed decoupled. Therefore, the inflow acoustic velocity fluctuations can be evaluated as

$$u'_{fuel}(\mathbf{x}_{ref}) = - \frac{p'(\mathbf{x}_{ref})}{\bar{\rho}_{fuel} \bar{c}_{fuel}}. \quad (31)$$

However, because of the configuration of the inner oxygen jet, there are reflection within the line. This phenomena is taken into account by the Helmholtz solver when computed the acoustic modes so that the oxygen acoustic inflow fluctuations can be computed using the modes' gradient in the longitudinal direction.

### Fuel inflow modulation

The inflow modulation of the fuel stream is supposed to directly impact the unsteady heat release per surface area due to local turbulent mixing enhancement. The fuel velocity fluctuation in the longitudinal direction is supposed to depend solely on the longitudinal abscissa and is written as

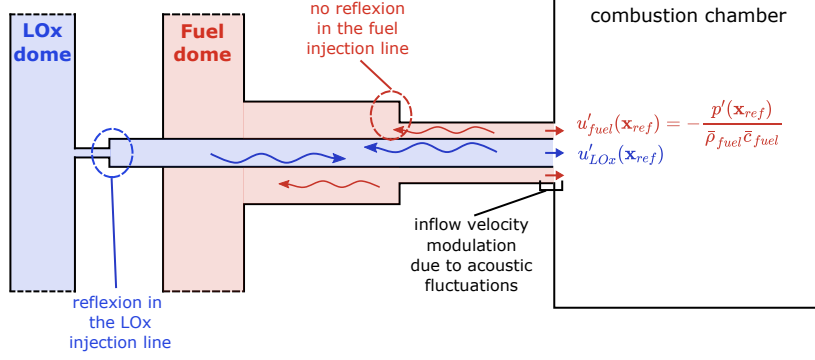


Figure 2: Coaxial injection unit of a typical LRE combustor similar to the BKD configuration with inflow velocity modulation due to acoustic fluctuations.

$$u'_{fuel}(\mathbf{x}, t) = \bar{u}_{fuel}(\mathbf{x}) \alpha(\mathbf{x}, t) \sin(\omega_m t - \kappa(\mathbf{x})\mathbf{x}), \quad (32)$$

with  $\bar{u}_{fuel}$  the averaged axial velocity in the annular jet,  $\alpha$  the local modulation amplitude and the wavenumber  $\kappa(x) = \omega_m / \bar{u}_{fuel}(\mathbf{x})$ . A proportionality is assumed between the local heat release rate and the local velocity:

$$\frac{\dot{q}'_l(\mathbf{x}, t)}{\dot{q}_{l0}(\mathbf{x})} \approx \frac{u'_{fuel}(\mathbf{x}, t)}{\bar{u}_{fuel}(\mathbf{x})}, \quad (33)$$

where  $\dot{q}_{l0}(\mathbf{x})$  is the linear heat release. Therefore

$$\dot{q}'_l(\mathbf{x}, t) = \alpha(\mathbf{x}, t) \dot{q}_{l0}(\mathbf{x}) \sin(\omega_m t - \kappa(\mathbf{x})\mathbf{x}). \quad (34)$$

The local amplitude is set to the amplitude of modulation at the outlet  $\mathbf{x}_{ref}$ , where the flame is positioned, as  $\alpha(\mathbf{x}, t) = \alpha(\mathbf{x}_{ref}, t)$ . Equation 34 is then solved numerically and a FTF is obtained, linking the total unsteady heat release of the flame  $\dot{Q}'$ , that is

$$\dot{Q}'(t) = \int_{\mathcal{V}} \dot{q}'(\mathbf{x}, t) dV \quad (35)$$

with the inflow velocity fluctuations at the injection unit outlet  $u'_{fuel}(\mathbf{x}_{ref})$ , as

$$\frac{\dot{Q}'(t) / \bar{Q}}{u'(\mathbf{x}_{ref}, t) / \bar{u}(\mathbf{x}_{ref})} = FTF(G, \Phi) \quad (36)$$

with  $G$  the gain and  $\Phi$  the phase. The phase  $\Phi$  corresponds to a time lag  $\tau$  and the gain  $G$  to an interaction index  $n$ . Manipulations on the combustion source term using Eq. 31, Eq. 35 and Eq. 36 lead, considering  $N_f$  flames, to a source term expressed as:

$$S_{fuelmod}^m(t) = \frac{1}{\Lambda_m} \sum_{i=1}^{N_f} \left[ \frac{(\gamma(\mathbf{x}_{ref,i}) - 1) n_i(\omega_m) \bar{Q}_i}{\bar{u}(\mathbf{x}_{ref,i})} \sum_{n=1}^M \frac{\hat{\eta}_n(t - \tau_i(\omega_m))}{(\bar{\rho} \bar{c})_{fuel}} \Psi_n(\mathbf{x}_{ref,i}) \Psi_m(\mathbf{x}_{ref,i}) \right]. \quad (37)$$

For the particular application to the BKD test bench (see Sec.6), the profiles of linear heat release  $\dot{q}_{l0}(\mathbf{x})$  along the flame length and of the fuel velocity  $\bar{u}_{fuel}(\mathbf{x})$  is shown in Fig. 3 and the FTF obtained numerically, for two typical loading points T65 and T131,<sup>7</sup> are shown in Fig. 4. A validation step of the implementation of Eq. 37 is made by computing the phase shift between the velocity and the heat release, and by comparing the amplitudes, on a 2D geometry, with a single flame. One can conclude that StaHF is correctly able to handle the FTF formulation.

## 5. Application to the NPCC test bench

### 5.1 NPCC overview

The NPCC test bench, for New Pressurized Coupled Cavities, was designed at EM2C laboratory,<sup>11</sup> as a cold flow experiment constituted of a dome and a chamber linked by three injection units. It has the possibility to change

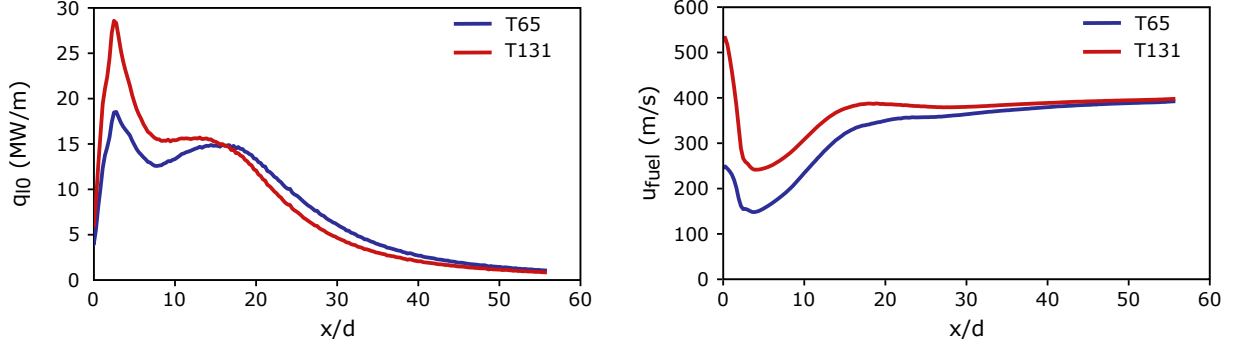


Figure 3: Linear heat release rate (left) and axial fuel velocity (right) of a BKD injection unit, with respect to the reduced distance  $x/d$  from the injection plate, and with  $d$  the injector diameter.

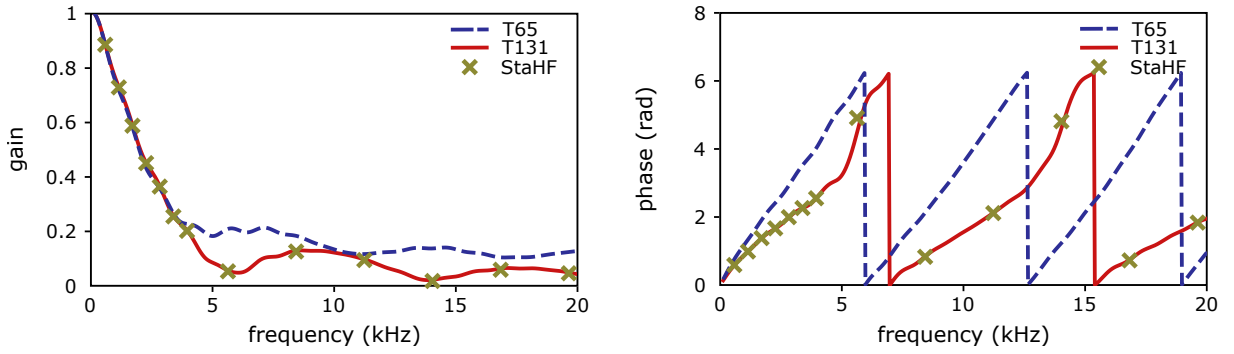


Figure 4: Gain and phase for the typical operating points T65 and T131 for the BKD combustor, obtained by the numerical resolution of Eq. 32.

the injection units head losses by adding diaphragms at the injectors' inlets. This results in the modification of the chamber/dome coupling. The exhaust chamber comprises two nozzles, upper and lower, and a very high amplitude modulator (VHAM),<sup>9</sup> which is a rotating toothed wheel that successively closes the upper and lower nozzles. This external modulation allows to drive acoustic oscillations within the chamber and excite targeted eigenmodes. Then it is possible to study how the dome responds to pressure fluctuations in the chamber and so to establish modeling of the injection dynamics. There is no combustion in the present case. Fig. 5 presents the NPCC geometry. It is possible to use different kinds of rotating wheels, depending on which phenomenon needs to be underlined. The fully perforated wheel allows exciting the cavities with a ramp of frequency so that by looking at the pressure response from sensors, one can deduce the eigenfrequencies experimentally. Also, it can drive and sustain the eigenmodes if the VHAM runs at the correct frequency. The second wheel, a half perforated one, gives some relaxation time for the pressure to decrease. Thus, one can estimate the damping coefficient of a specific mode by looking at the exponential decrease of pressure signals.

Gonzalez-Flesca<sup>11</sup> provided the experimental measurements of the pressure oscillations in the dome and in the chamber when the VHAM excites the 1T, 1T1L and 1T2L modes. Using the half-perforated wheel, the global acoustic damping coefficient was also estimated. Later, Marchal<sup>36</sup> retrieved the experimental results with a 3D LES of the test bench.

The VHAM has been modeled using the reduced order framework<sup>9</sup> so that the corresponding source term is

$$S_{VHAM}^m = \frac{\dot{m}_{mod}}{2\Lambda_m} \omega_e \bar{c}^2 (\Psi_m(\mathbf{x}_1) - \Psi_m(\mathbf{x}_2)) \sin(\omega_e t), \quad (38)$$

with  $\dot{m}_{mod}$  the modulated mass flow rate,  $\omega_e$  the excitation frequency and  $\mathbf{x}_1$  and  $\mathbf{x}_2$  the position of the nozzles. The value of  $\dot{m}_{mod}$  differs from the total mass flow rate measured in the experiment ( $3.1g.s^{-1}$ ), since leaks are present near the nozzle that reduce the modulated mass flow rate to  $\dot{m}_{mod} \approx 0.84g.s^{-1}$  as shown in Marchal.<sup>36</sup>

The acoustic modes and frequencies are computed using the AVSP<sup>14</sup> solver, for a mean pressure  $\bar{p} = 3.5bar$ , a mean density  $\bar{\rho} = 4.14kg.m^{-3}$  and temperature  $\bar{T} = 293K$ . Fig.5 shows the 1T, 1T1L and 1T2L modes with the corresponding frequencies. The numerical results obtained by Marchal<sup>36</sup> are also shown on Fig. 5. Agreement between

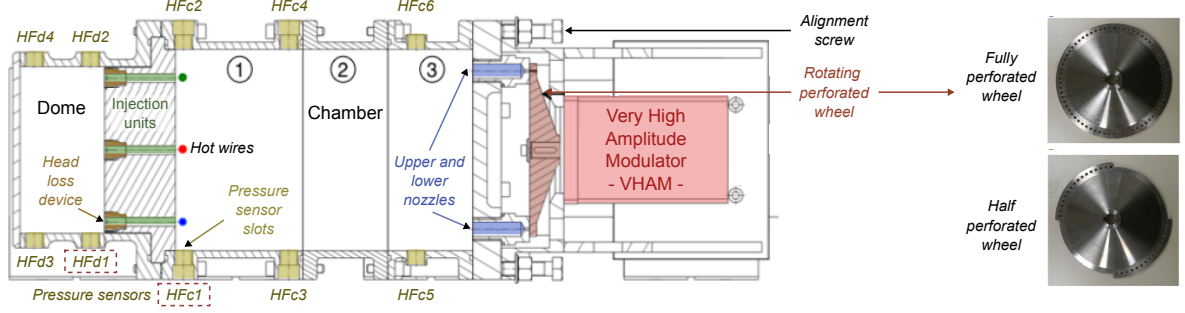


Figure 5: New Pressurized Coupled Cavities (NPCC) test bench.<sup>11</sup> It runs cold flow, the air passes from the dome to the chamber through 3 injection units with variable head losses and exits via two nozzles that are successively closed by a rotating toothed wheel (Very High Amplitude Modulator) to impose a specific acoustic excitation frequency. Pressure sensors are deployed along the test bench.

LES and experiment is very good, so that LES can also be used for comparison with ROM.

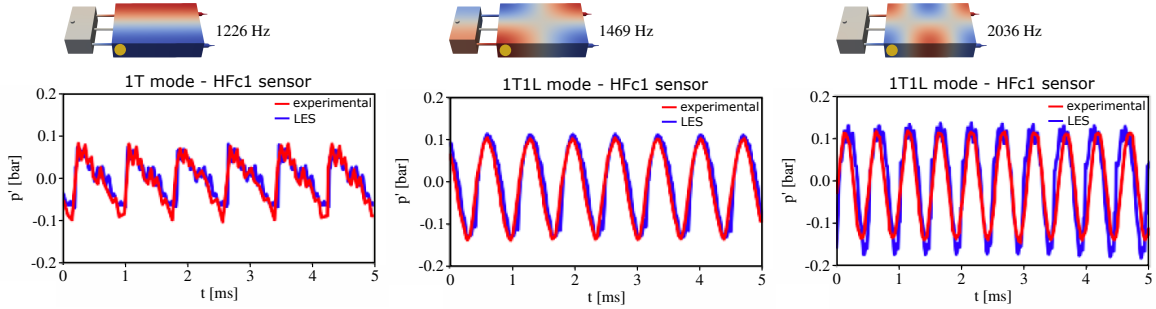


Figure 6: 1T, 1T1L and 1T2L modes' structure and frequency, computed using the AVSP solver, for a sound speed of  $\bar{c} = 343m.s^{-1}$ , along with experimental<sup>11</sup> and LES<sup>36</sup> results of each mode excitation.

A continuous modulation of the three proposed acoustic modes is performed, by imposing  $\omega_e = \omega_m$ , and comparisons are made with experimental<sup>9</sup> and LES<sup>36</sup> results in the following part of this section.

## 5.2 Evaluation of the damping coefficients

First of all, an evaluation of the damping phenomena reviewed in Sec. 3 is made. The viscous and thermal losses are computed using Eq. 14 and Eq. 17 with a viscosity  $\nu = 4.82 \times 10^{-6}m^2.s^{-1}$  and a thermal diffusivity  $D_{th} = 12.0 \times 10^{-6}m^2.s^{-1}$ . Formulations accounting for the near-wall turbulence influence are available,<sup>16</sup> but in the present application, the turbulence intensity is too weak to increase the viscous and thermal losses. The representative impedance to be applied at the nozzles' outlet is computed using the ANOZZLE<sup>37</sup> solver, supposing a choked outlet, that gives the impedance with respect to the frequency. Then, Eq. 20 is applied at the outlet. Using the LES carried out by Marchal,<sup>36</sup> an estimation of the RMS velocity and of the turbulent dissipation rate is made within the domain, and the formulation Eq. 26 is used to quantify the turbulence acoustic interaction. Finally, the conversion of acoustics into vorticies at the injection units' outlet is evaluated using  $a = 3mm$ ,  $d = 50mm$ ,  $L = 58mm$ ,  $u_0 = 10m.s^{-1}$ . Table 1 gives the damping rates for each phenomenon. The viscous and thermal losses are preponderant, the nozzles losses are negligible mainly due to the small section of the nozzles, the acoustic turbulence interaction is also negligible and the perforated plate losses are not negligible but modest.

## 5.3 Linear hypothesis application

For each mode, the StaHF differential equation writes, in a simple form,

$$\ddot{\eta}_m(t) + 2\sigma_m\dot{\eta}_m(t) + \omega_m^2\eta_m(t) = S_{VHAM}^m, \quad (39)$$

Table 1: Damping rates ( $s^{-1}$ ) associated with each damping phenomenon modeled, for the 1T, 1T1L and 1T2L modes.

	Frequency	Thermal losses	Viscous losses	Nozzle losses	Turbulence interaction	Perforated plate losses
<b>1T</b>	1226.0 Hz	$3.45s^{-1}$	$3.45s^{-1}$	$10^{-3}s^{-1}$	$10^{-8}s^{-1}$	$0.40s^{-1}$
<b>1T1L</b>	1468.8 Hz	$4.48s^{-1}$	$4.78s^{-1}$	$10^{-3}s^{-1}$	$10^{-8}s^{-1}$	$0.46s^{-1}$
<b>1T2L</b>	2036.3 Hz	$5.19s^{-1}$	$5.89s^{-1}$	$10^{-3}s^{-1}$	$10^{-8}s^{-1}$	$0.19s^{-1}$

with  $\sigma_m$  the sum of all the contribution given in Table 1. The damping is linear and the limit cycle is a competition between the damping coefficient  $\sigma_m$  and the VHAM modulation. The result of the StaHF simulation are compared to the experimental results in Fig. 7 and Fig. 8. Fig. 7 shows on the left the total signal along the experimental limit cycle amplitude, and on the right a focus on a  $5ms$  window where the two signals are superimposed. It can be seen that StaHF shows a correct amplitude, very satisfying for a reduced-order code without any adjustment parameters. However, the shape of the experimental curve is not reproduced. This particular shape is caused by the nonlinear nature of the 1T modulation for this amplitude of modulation. As shown by Marchal,<sup>36</sup> the modulation amplitude is strong enough to trigger a nonlinear acoustic response. There is a steepening of the acoustic wave,<sup>10</sup> as a shock formation, and the pressure signal is no longer a pure harmonic signal composed of solely the 1T contribution but feature several subharmonics. This steepening explains the shape of the signal. A nonlinear representation of the damping is therefore proposed in the next section.

The 1T1L and 1T2L modulations are also performed, and the comparisons with experiments are given in Fig. 8. The signals show a more classical sinusoidal form. It was pointed out that these modulations are less subject to a nonlinear acoustics behavior, and the fundamental mode is the dominating one, with only a limited response of the harmonics. As for the 1T case, the 1T1L and 1T2L limit cycle amplitudes are well retrieved by the reduced order model.

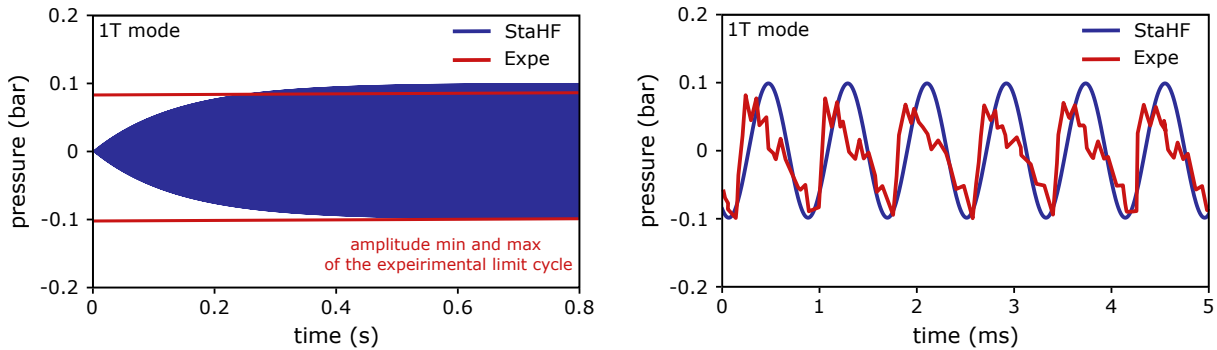


Figure 7: Comparison of the 1T mode pressure response between the reduced-order simulation and the experimental results, using a linear damping formulation.

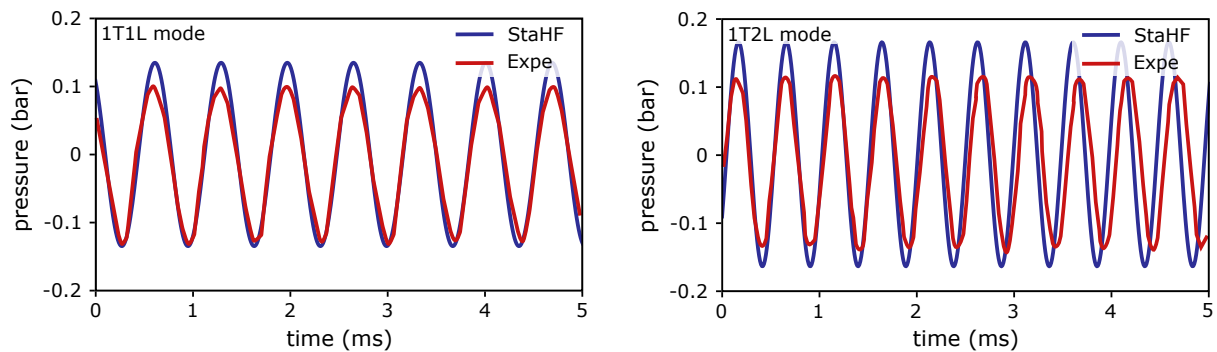


Figure 8: Comparison of the 1T1L (left) and (1T2L) mode pressure response between the reduced-order simulation and the experimental results, using a linear damping formulation.

## 5.4 Modeling the nonlinear acoustics

In this part, the impact of acoustic nonlinearities on the fundamental mode damping is modeled. The modeling is based on the theoretical work depicted in Garrett<sup>38</sup> and Hargrove.<sup>39</sup> This work shows that the velocity amplitude evolution  $|C_n|$  of the harmonics of a propagating wave due to nonlinear effects can be properly described by the following relation:

$$|C_n| = \frac{2}{n\sigma} J_n(\sigma), \quad (40)$$

with  $J_n$  the  $n^{\text{th}}$  Bessel function and  $\sigma$  a scaled distance.<sup>38</sup> Focusing on the fundamental mode, assuming that relevant damping occurs at the inception point (position where the shock is formed), it is possible to express the pressure amplitude derivative (thus the damping) in terms of pressure fluctuation amplitude:

$$\frac{dA_p}{dt} = -\Gamma\omega \frac{p'^2}{4\rho c^2}, \quad (41)$$

where  $A_p$  is the amplitude of the mode in terms of pressure and  $\Gamma$  is the Grüneisen parameter. It leads to the StaHF equation with nonlinear damping term:

$$\ddot{\eta}_m(t) + 2\sigma_m \dot{\eta}_m(t) + 2\beta_m |\eta_m(t)| \dot{\eta}_m(t) + \omega_m^2 \eta_m(t) = S_{VHAM}^m, \quad (42)$$

with  $\beta_m$  the nonlinear coefficient found as

$$\beta_m = \frac{1}{0.64} \frac{\Gamma\omega_m}{4\rho c^2}. \quad (43)$$

with  $\Gamma = 6/5$  for air and the coefficient  $1/0.64$  arises from the extraction of the mode amplitude from the harmonic signal used in StaHF. Fig. 9 shows the total signal and a  $2ms$  windowed view of the StaHF results along with the LES prediction. The LES is the computed signal that has been filtered around the 1T frequency to isolate the fundamental mode, which in this case is the 1T mode. Note that on the reduced-order computation, the thermal losses have been set aside since the LES uses an adiabatic wall condition. The results are found to be in very good agreement with the reference, suggesting the model properly captures the physical phenomenon. Harmonics source terms are not accounted for for the moment and are the subject of current researches.

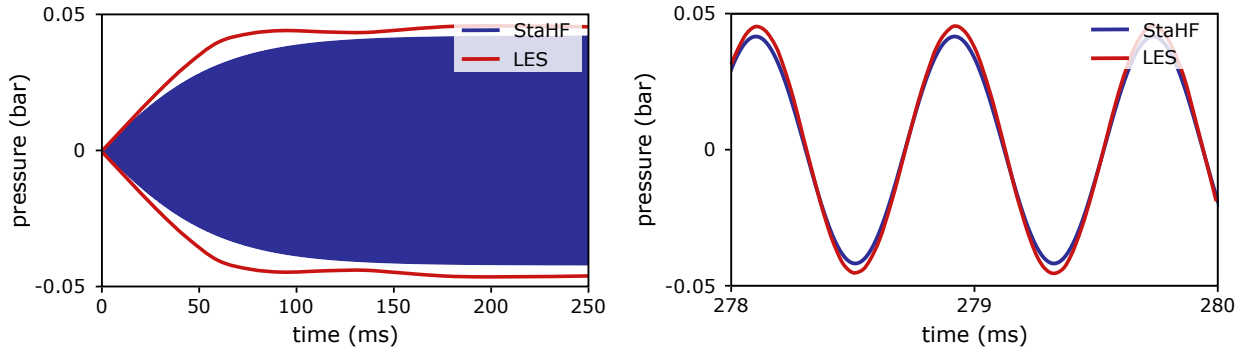


Figure 9: Comparison of the 1T mode pressure response between the reduced-order simulation and the LES fitted results, using a nonlinear damping formulation.

## 6. Application to the BKD test bench

The BKD combustor<sup>5</sup> is a reduced-scale  $LO_x/H_2$  liquid rocket engine equipped with 42 shear injection units operated at DLR Lampoldshausen. We propose to apply the ROM methodology to the T65 and T131<sup>7</sup> loading points. The injection mass flow rates of propellant and oxygen temperature are the same for both loading points, with  $\dot{m}_{LO_x} = 5.8 kg.s^{-1}$ ,  $\dot{m}_{H_2} = 5.8 kg.s^{-1}$  and  $T_{LO_x} = 107.6K$ . The temperature of hydrogen is however different:  $T_{H_2} = 65K$  for the T65 case and  $T_{H_2} = 131.7K$  for the T131 case. From experiment measurements,<sup>40</sup> it is expected that case T131 features a dominating 1T mode, while case T65 features a dominating 2T mode.

The mean sound speed field is extracted from LES<sup>7</sup> and eigenmodes are computed using the AVSP solver.<sup>14</sup> Table 2 gives the frequency found for the 1T, 1T1L, 1T2L, 2T, 3T and 1R modes for both loading points and Fig. 10

shows the spatial shape of these modes. The shapes are quite similar for both T65 and T131, this is why they are not shown for T131.

Table 2: Frequencies (Hz) of the 1T, 1T1L, 1T2L , 2T, 3T and 1R modes of the BKD for the T65 and T131 loading points, with the AVSP solver.

	1T	1T1L	1T2L	2T	3T	1R
<b>T65</b>	9582 Hz	11732 Hz	12823 Hz	15722 Hz	21163 Hz	21613 Hz
<b>T131</b>	10568 Hz	12164 Hz	13254 Hz	17108 Hz	23229 Hz	23661 Hz

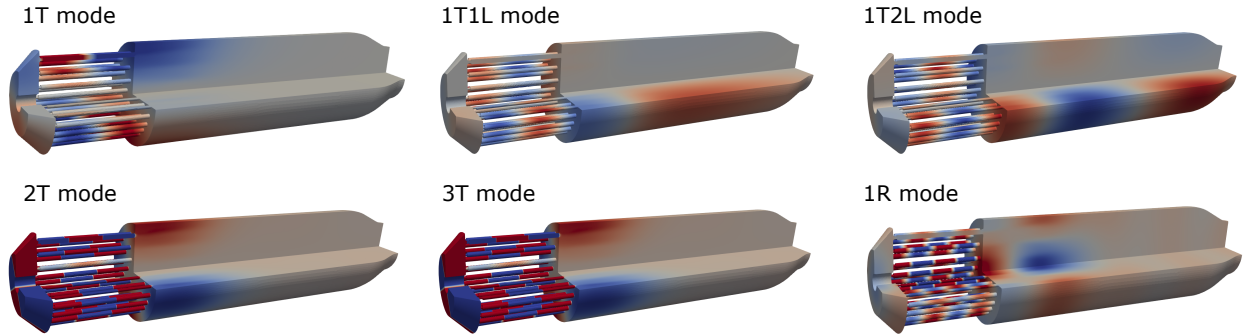


Figure 10: 1T, 1T1L, 1T2L, 2T, 3T and 1R modes of the BKD combustor<sup>5</sup> computed with AVSP<sup>14</sup> for the T65 case.<sup>7</sup>

The modes frequencies are compared to the ones observed in the LES using the pressure PSD.<sup>7</sup> Figure 11 shows the PSD based on numerical simulations<sup>7</sup> and the frequencies of the 1T, 2T, 3T and 1R modes found with AVSP. The frequencies are well-retrieved, especially for the 1T and 2T modes.

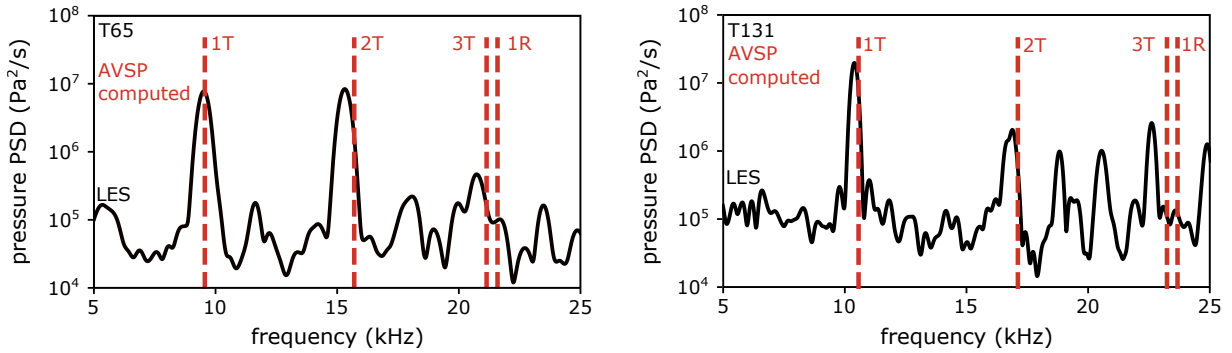


Figure 11: PSD of the pressure temporal signal from LES<sup>7</sup> for T65(left) and T131(right) cases, and AVSP results (dashed lines).

To evaluate the damping contribution of each phenomenon described in of Sec. 3, the viscosity  $\nu$  and thermal diffusivity  $D_{th}$  are also extracted from the LES.<sup>7</sup> The impedance applied at the nozzle outlet is obtained using the ANOZZLE tool,<sup>37</sup> supposing a non-compact nozzle. Tables 3 and 4 show the damping coefficients obtained. The interaction with the turbulence is set to 0 since the different evaluations made here indicate that this phenomenon is probably negligible. The viscous losses are more important than the thermal losses, and the nozzle losses grow when longitudinal components are presents. The particular behavior of the viscous losses with respect to the mode is due to the level of acoustic in the injection lines. For instance, for the 1T mode of T131, the acoustics in the injection lines is more important, compared to the acoustic in the chamber, than for the T65. Therefore, the total wall surface of the injection lines being more important than the wall surface of the chamber, the modes experiencing higher response in the injectors have more viscous losses. The perforated plate losses have been evaluated for the H<sub>2</sub> injectors, supposing no reflection in the dome. The damping obtained is important, but it is interesting to note that it is modest, on one hand, for the 2T mode of T65 and on the other hand, for the 1T mode of T131. It is explained by the acoustic mode intensity in the chamber compared to the intensity in the injection lines.

The growth rate associated with each combustion terms is also evaluated. The pressure response leads to growth rates, because the heat release is in phase with the acoustic. But it is not enough to counter-balance the damping phenomena alone. The coaxial response source term modeled with the FTF and the profiles of Fig. 4 acts, for most modes, as a positive source term.

The balance between the damping and the combustion terms is also given. For both loading points, the damping exceed largely the destabilizing effects, so that all the modes are stable. Some phenomena have not been modeled, as the transverse flames motion<sup>9</sup> or the coaxial  $LO_x$  inflow modulation that could trigger instabilities.

Table 3: Damping and growth rates ( $s^{-1}$ ) for the BKD T65 case, obtained with StaHF.

	damping					combustion		balance
	viscous losses	thermal losses	nozzle losses	turbulence interaction	perforated plate	pressure response	H2 coaxial modulation	
<b>1T</b>	367.6	10.0	$10^{-2}$	0	4456.5	-3619.4	-810.8	403.9
<b>1T1L</b>	101.7	8.4	41.2	0	1506.0	-1481.7	-162.8	54.0
<b>1T2L</b>	73.0	8.7	357.2	0	1457.7	-1424.9	-257.1	571.8
<b>2T</b>	1703.1	20.4	$10^{-3}$	0	30.7	-2.9	0.5	1751.8
<b>3T</b>	1856.7	23.9	$10^{-2}$	0	75.4	-262.7	-20.9	1672.4
<b>1R</b>	1103.7	18.4	64.2	0	1082.7	-1626.7	-230.3	476.1

Table 4: Damping and growth rates ( $s^{-1}$ ) for the BKD T131 case, obtained with StaHF.

	damping					combustion		balance
	viscous losses	thermal losses	nozzle losses	turbulence interaction	perforated plate	pressure response	H2 coaxial modulation	
<b>1T</b>	1351.4	15.7	$10^{-2}$	0	323.6	-292.8	-19.5	1378.4
<b>1T1L</b>	70.0	8.2	102.2	0	2118.6	-1337.9	-257.0	704.1
<b>1T2L</b>	90.1	9.1	421.2	0	2911.9	-1785.9	-181.8	1464.6
<b>2T</b>	383.2	14.2	10.9	0	6147.3	-3809.2	559.4	3305.8
<b>3T</b>	727.0	18.7	139.2	0	6500.0	-3127.7	-668.8	3588.4
<b>1R</b>	666.2	13.9	9.2	0	6229.5	-2573.0	-667.3	3678.5

## 7. Conclusion

A reduced-order strategy based on a modal decomposition of the pressure oscillations has been presented. Models to account for some of the acoustic damping phenomena has been developed, as the viscous and thermal losses, the nozzle losses, the turbulence acoustic interaction or the perforated plate losses. A combustion model has been derived in order to include a flame transfer function into the low order code.

A first application to the NPCC test bench shows good agreements with the experiments. A nonlinear damping model is proposed to explain the particular shape of the 1T mode. Using this nonlinear damping representation, the LES filtered at the excitation frequency results are retrieved.

Then, the T65 and T131 loading points of the BKD combustor are simulated and compared with LES results. Results shows that the damping rates evaluated exceed the growth rates. Therefore we believe that further models have to be included into the simulation, as the traverse flames motion or the unsteady heat release due to the inflow  $LO_x$  modulation.

## 8. Acknowledgments

This work is part of an ongoing PhD thesis at EM2C laboratory, cofunded by CNES, the French National Space Agency and ArianeGroup. A part of this work was performed using HPC resources from the mesocentre computing center of Ecole CentraleSupélec and Ecole Normale Supérieure Paris-Saclay supported by CNRS and Région Ile-de-France.

## References

- [1] L. Crocco and S.-I. Cheng. Theory of combustion instability in liquid propellant rocket motors. *Butterworths Scientific Publications*, 1956.
- [2] D.T. Harrje and F.H. Reardon. Liquid propellant rocket combustion instability. *Technical Report SP-194*, NASA, 1972.
- [3] J.C. Oefelein and V. Yang. Comprehensive review of liquid-propellant combustion instabilities in F-1 engines. *Journal of Propulsion and Power*, 9(5):657–677, 1993.
- [4] Y. Méry, L. Hakim, P. Scoufflaire, L. Vingert, S. Ducruix, and S. Candel. Experimental investigation of cryogenic flame dynamics under transverse acoustic modulations. *Comptes Rendus Mécanique*, 341(1-2):100–109, 2013.
- [5] J.S. Hardi, T. Traudt, C. Bombardieri, M. Börner, S.K. Beinke, W. Armbruster, P.N. Blanco, F. Tonti, D. Suslov, B. Dally, and M. Oswald. Combustion dynamics in cryogenic rocket engines: Research programme at DLR Lampoldshausen. *Acta Astronautica*, 147:251–258, 2018.
- [6] A. Urbano, L. Selle, G. Staffelbach, B. Cuenot, T. Schmitt, S. Ducruix, and S. Candel. Exploration of combustion instability triggering using Large Eddy Simulation of a multiple injector liquid rocket engine. *Combustion and Flame*, 169:129–140, 2016.
- [7] T. Schmitt and G. Staffelbach. REST HF-9 test case: Large-Eddy Simulation of DLR’s BKD configuration. *9th European Conference for Aeronautics and Aerospace Sciences (EUCASS)*, 2022.
- [8] C. Laurent, M. Bauerheim, T. Poinso, and F. Nicoud. A novel modal expansion method for low-order modeling of thermoacoustic instabilities in complex geometries. *Combustion and Flame*, 206:334–348, 2019.
- [9] Y. Méry. Mécanismes d’instabilités de combustion haute-fréquence et application aux moteurs-fusées. *Ph.D. thesis, Ecole Centrale Paris*, 2010.
- [10] F.E.C. Culick. Unsteady Motions in Combustion Chambers for Propulsion Systems. *NATO Research and Technology Organization*, AC/323 (AVT-039) TP/10, 2006.
- [11] M. Gonzalez-Flesca. Simulation, experimentation and modeling contributions to the analysis of high frequency combustion instabilities in liquid propellant rocket engines. *PhD Thesis, CentraleSupélec, Université Paris-Saclay*, 2016.
- [12] F.E.C. Culick. Stability of high-frequency pressure oscillations in rocket combustion chambers. *AIAA Journal*, 1(5):1097–1104, 1963.
- [13] S. Evesque and W. Polifke. Low-order acoustic modelling for annular combustors: Validation and inclusion of modal coupling. *Proceedings of the ASME Turbo Expo 2002: Power for Land, Sea and Air*, (GT-2002-30064), 2002.
- [14] F. Nicoud, L. Benoit, C. Sensiau, and T. Poinso. Acoustic Modes in Combustors with Complex Impedances and Multidimensional Active Flames. *AIAA Journal*, 45:426–441, 2007.
- [15] A. Fougny, T. Schmitt, and D. Ducruix. Low order modeling of high frequency combustion instabilities in liquid rocket engines. *Proceedings of Space Propulsion 2021, Conference Paper*, 2021.
- [16] A. Fougny, T. Schmitt, and D. Ducruix. Analysis and low order modeling of the acoustic damping for high-frequency combustion instabilities prediction in liquid rocket engines. *Proceedings of Space Propulsion 2022, Conference Paper*, 2022.
- [17] F.E.C. Culick. Nonlinear behavior of acoustic-waves in combustion chambers - II. *Acta Astronautica*, 3(9-10):735–757, 1976.
- [18] G. Searby, A. Nicole, M. Habiballah, and E. Laroche. Prediction of the Efficiency of Acoustic Damping Cavities. *Journal of Propulsion and Power*, 24(3):516–523, 2008.
- [19] F. Mbailassem, E. Gourdon, Q. Leclere, E. Redon, and T. Cambonie. Sound absorption prediction of linear damped acoustic resonators using a lightweight hybrid model. *Applied Acoustics*, 150:14–26, 2019.

- [20] R.F. Lambert. A Study of the Factors Influencing the Damping of a Acoustical Cavity Resonator. *The Journal Of the Acoustical Society of America*, 25(6):1068–1083, 1953.
- [21] M.J. Lighthill. On the energy scattered from the interaction of turbulence with sound or shock waves. *Mathematical Proceedings of the Cambridge Philosophical Society*, 49(3):531–551, 1953.
- [22] M.S. Howe. On wave scattering by random inhomogeneities, with application to the theory of weak bores. *Journal of Fluid Mechanics*, 45(4):785–804, 1971.
- [23] D.T. Noir and A.R. George. Absorption of sound by homogeneous turbulence. *Journal of Fluid Mechanics*, 86(3):593–608, 1978.
- [24] S.C. Crow. Visco-Elastic Character of Fine-Grained Isotropic Turbulence. *Physics of Fluids*, 10(7), 1967.
- [25] W.C. Reynolds and A.K.M.F. Hussain. The mechanics of an organized wave in turbulent shear flow. Part 3. Theoretical models and comparisons with experiments. *Journal of Fluid Mechanics*, 54(2):263–288, 1972.
- [26] M.S. Howe. On the Absorption of Sound by Turbulence and Other Hydrodynamic Flows. *IMA Journal of Applied Mathematics*, 32:187–209, 1984.
- [27] B.-T. Chu and L.S.G. Kovaszny. Non-linear interactions in a viscous heat-conduction compressible gas. *Journal of Fluid Mechanics*, 3(5):494–514, 1958.
- [28] E. Gullaud and F. Nicoud. Effect of Perforated Plates on the Acoustics of Annular Combustors. *AIAA Journal*, 50(12), 2012.
- [29] C. Lioi, D. Ku, and V. Yang. Linear Acoustic Analysis of Main Combustion Chamber of an Oxidizer-Rich Staged Combustion Engine. *Journal of Propulsion and Power*, 34(6):1505–1518, 2018.
- [30] M.S. Howe. On the theory of unsteady high Reynolds number flow through a circular aperture. *Proceedings of the Royal Society of London*, 366(1725):205–223, 1979.
- [31] A. Scarpato, N. Tran, S. Ducruix, and T. Schuller. Modeling the damping properties of perforated screens traversed by a bias flow and backed by a cavity at low Strouhal number. *Journal of Sound and Vibration*, 331(2):276–290, 2012.
- [32] A. Scarpato, S. Ducruix, and T. Schuller. Optimal and off-design operations of acoustic dampers using perforated plates backed by a cavity. *Journal of Sound and Vibration*, 332(20):4856–4875, 2013.
- [33] X. Jing and X. Sun. Effect of plate thickness on impedance of perforated plates with bias flow. *AIAA Journal*, 38(9):1573–1578, 2000.
- [34] R. Nez, T. Schmitt, M. Gonzalez-Flesca, S. Candel, and S. Ducruix. Response of a transcritical coaxial flame to fuel injection rate modulations: analysis and low-order modeling of the generation of unsteady heat release rate. *7th European Conference for Aeronautics and Aerospace Sciences (EUCASS)*, 2017.
- [35] C. Laurent, G. Staffelbach, F. Nicoud, and T. Poinso. Heat-release dynamics in a doubly-transcritical LO<sub>2</sub>/LCH<sub>4</sub> cryogenic coaxial jet flame subjected to fuel inflow acoustic modulation. *Proceedings of the Combustion Institute*, 38(4):6375–6383, 2021.
- [36] D. Marchal, T. Schmitt, and S. Ducruix. Numerical characterization of the damping in a cold-flow experiment with coupled cavities. *Proceedings of Space Propulsion 2020, Conference Paper*, 2021.
- [37] F. Nicoud and K. Wieczorek. About the zero Mach number assumption in the calculation of thermoacoustic instabilities. *International journal of spray and combustion dynamics*, 1(1):67–112, 2009.
- [38] S.L. Garrett. Understanding Acoustics: An Experimentalist’s View of Sound and Vibration. Second Edition. *Springer Nature*, 2020.
- [39] L.E. Hargrove. Fourier Series for the Finite Amplitude Sound Waveform in a Dissipationless Medium. *Journal of the Acoustical Society of America*, 32, 1960.
- [40] S. Gröning, J. Hardi, D. Suslov, and M. Oschwald. Influence of hydrogen temperature on the stability of a rocket engine combustor operated with hydrogen and oxygen: A new hydrogen temperature ramping experiment. *CEAS Space Journal*, 9(1):59–76, 2017.